INTERNATIONAL JOURNAL FOR NUMERICAL METHODS IN ENGINEERING
Int. J. Numer. Meth. Engng (2015)
Published online in Wiley Online Library (wileyonlinelibrary.com). DOI: 10.1002/nme.5169

A three-dimensional surface stress tensor formulation for simulation of adhesive contact in finite deformation

Houfu Fan and Shaofan Li*,†

Department of Civil and Environmental Engineering, the University of California, Berkeley, CA 94720, USA

SUMMARY

A three-dimensional surface adhesive contact formulation is proposed to simulate macroscale adhesive contact interaction characterized by the van der Waals interaction between arbitrarily shaped deformable continua under finite deformation. The proposed adhesive contact formulation uses a double-layer surface integral to replace the conventional double volume integration to compute the adhesive contact force vector. Considering nonlinear finite deformation, we have derived the surface stress tensor and the corresponding tangent stiffness matrix in a Galerkin weak formulation. With the surface stress formulation, the adhesive contact problems are solved in the framework of nonlinear continuum mechanics by using the standard Lagrange finite element method. Surface stress tensors are formulated for both interacting bodies. Numerical examples show that the proposed surface contact algorithm is accurate, efficient, and reliable for three-dimensional adhesive contact problems of large deformations for both quasi-static and dynamic simulations.

Received 5 March 2015; Revised 1 August 2015; Accepted 5 November 2015

KEY WORDS: adhesive contact; Derjuguin approximation; finite element method; finite deformation; surface stress tensor; van der Waals interaction

1. INTRODUCTION

The Hertz contact between deformable continua under finite deformation has been extensively studied in the computational contact mechanics [1, 2]. On the other hand, the adhesive contact problems that are related to colloidal physics and chemistry have become more and more important and useful in engineering applications, e.g. [3–7], among many others. Generally speaking, there is lack of efficient modeling and simulation tools for analyzing such problems at macroscale.

In the literature, there are several theoretical models for adhesive contact at microscale or nanoscale, such as the Johnson–Kendall–Roberts model [8] and the Derjaguin–Muller–Toporov model [9]. Although these models have proven successful to a certain degree in engineering applications, they have some intrinsic limitations, by either assuming infinitesimal deformations, contacting bodies with special geometries, or requiring one of the contacting body to be rigid and hence substantially simplifying the computational treatment. Contact interaction of two bodies originates from the inter-body interaction of individual atoms or molecules. At atomic scale, this type of interaction can always be simulated by using first-principle calculation or empirical potential-based molecular dynamics [10–12], which is the predominant case in nanomechanics research such as the studies of DNA strands and proteins [13], flexible nanotubes [14, 15], and atomic force microscopy [16–18], among others. However, most molecular dynamics studies mainly focus on the general principles, instead of practical applications in engineering, because of the limitation of computer power and storage capacity. Even in the foreseeable future, it may not be a practical approach, if not impossible, to use first-principle-based calculations to model, predict, and design macroscale engineering systems that are involved with adhesive contact.

*Correspondence to: Shaofan Li, Department of Civil and Environmental Engineering, the University of California, Berkeley, CA 94720, U.S.A.
†E-mail: shaofan@berkeley.edu

To capture small-scale adhesive contact interaction, one must incorporate microscopic interactions of the underlying atoms/molecules into macroscale continuum mechanics and formulate the problem in a multiscale framework that takes into account both molecular interaction and nonlinear continuum mechanics kinematics. Moreover, to be successful at solving macroscale problems, one has to keep the computation cost to an acceptable level. In [19, 20], a so-called coarse-grained contact model (CGCM) is proposed to study the adhesive contact between two arbitrary deformable bodies at nanoscale/microscale. Similar to a classical Barrier contact method [1, 21], the CGCM characterizes the small-scale contact by introducing the inter-body interaction potentials between atoms/molecules into the total potential energy of the system. However, if one directly applies the body-to-body atomistic interaction potential to the system, the computational cost would be so large that no practical engineering problem can be solved. Meanwhile, the original work of the CGCM only serves to describe the adhesive contact of two arbitrarily shaped bodies in two-dimensional space. In [22], the present authors have adopted a surface adhesive contact formulation proposed in [23, 24] and extend it to the case of finite deformation in the framework of nonlinear continuum mechanics, which is suitable for both two-dimensional and three-dimensional arbitrarily shaped deformable interacting bodies. In the proposed surface formulation, the double-layer volume integral describing the contact interaction (energy, force vector, and matrix) is converted into a double-layer surface integral through a mathematically consistent approach that employs the divergence theorem and a special partitioning technique. In that work, the proposed surface contact formulation is employed to analyze two-dimensional problems for both quasi-static and explicit dynamic simulations. The present paper serves as an extension of the previous work by investigating contact interaction problems in three-dimensional space. In addition, through analytical integrations, surface stress tensors for rigid bodies with simple geometries are obtained in explicit expressions. With surface stress tensors, the evaluation of the contact interaction force and the corresponding contact stiffness matrix can be highly simplified.

The paper is organized into five sections. In Section 2, an overview of the surface adhesive contact formulation in the framework of nonlinear continuum mechanics is offered. In Section 3, the surface stress tensor and its possible applications are discussed. In particular, the surface stress tensor for a perfect sphere is presented. Section 4 discusses the Galerkin weak formulation and finite element implementation of the adhesive contact problem. In Section 5, the contact tangent stiffness matrices are derived. In Section 6, several numerical examples are offered. Conclusions are drawn in Section 7.

2. AN OVERVIEW OF THE SURFACE CONTACT FORMULATION

In this section, the proposed surface formulation of adhesive contact is presented in the framework of nonlinear continuum mechanics. We first consider two interacting bodies 1 and 2, as shown in Figure 1. Subjected to certain boundary conditions (not shown in the figure) and the inter-body contact interactions, the two bodies originally occupying the physical domains Ω_{10}, Ω_{20} deform and evolve to Ω_1, Ω_2 in the current configuration. Correspondingly, the boundaries (surfaces) and unit out-normals of the two bodies change from $\partial\Omega_{10}, \partial\Omega_{20}$ and $\mathbf{N}_1, \mathbf{N}_2$ to $\partial\Omega_1, \partial\Omega_2$ and $\mathbf{n}_1, \mathbf{n}_2$. If the system is conservative, the total potential energy of the system can be written as

$$\Pi^{total} = \sum_{I=1}^{2} \left(\Pi^{int,I} + \Pi^{ext,I}\right) + \Pi^{C}, \tag{1}$$

where $\Pi^{int,I}, I = 1, 2$ are the usual internal potential energy of standard continua, which are involved with stresses and strains, and $\Pi^{ext,I}, I = 1, 2$ are the external potential energy of standard continua, which are involved with external body force and external traction forces. One may use the principle of virtual work to derive the governing equations of the aforementioned adhesive contact problem, but the additional adhesive interaction potential energy, Π_c, will make this a non-standard boundary value problem because it produces a body-to-body interaction integral that is dependent not only on molecular adhesion but also on the deformations of the two bodies.

DOI: 10.1002/nme

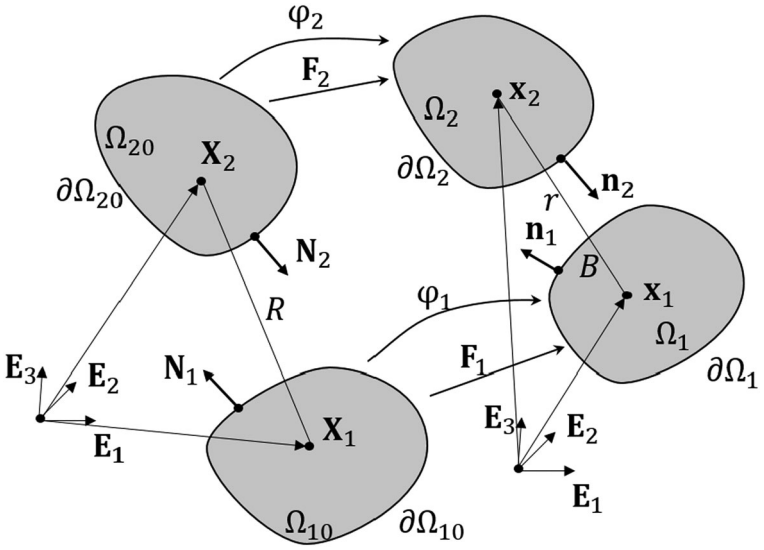

Figure 1. Schematic description of the adhesive contact model.

To see this clearly, we assume that the contact interaction between the two bodies is described by the interaction of material particles inside the bodies. The interaction between two particles located at $\mathbf{x}_1 \in \Omega_1$ and $\mathbf{x}_2 \in \Omega_2$ can be described by a two-point potential $\phi(r)$, where $r = |\mathbf{x}_1 - \mathbf{x}_2|$. Practically, this potential can be of any form suitable to the problem considered. In this work, we choose the 12-6 Lennard-Jones potential to represent such adhesive or cohesive interaction

$$\phi(r) = \varepsilon \left[\left(\frac{\sigma_0}{r}\right)^{12} - 2\left(\frac{\sigma_0}{r}\right)^{6} \right], \tag{2}$$

where ε is the potential well and σ_0 is the equilibrium distance. The term r^{-12} describes the short-range Pauli repulsion effect, which prevents the two particles from being too close. The total interaction energy of the homogenized interaction energy for the adhesive contact can then be written as

$$\Pi^C = \int_{\Omega_1} \int_{\Omega_2} \beta_1 \beta_2 \phi(r) dv_2 dv_1, r = |\mathbf{x}_1 - \mathbf{x}_2|, \tag{3}$$

where β_1 and β_2 represent the current particle densities located at points $\mathbf{x}_1 \in \Omega_1$ and $\mathbf{x}_2 \in \Omega_2$.

With the total interaction energy Π^C, one can directly take the first variation and identify the corresponding contact interaction forces and hence derive the contact stiffness matrix [19, 20]. However, one may notice that Equation (3) involves a double-layer integral over the volumes of the two bodies, and so do the corresponding expressions for the contact forces and stiffness matrix. The double-layer volume integral requires huge computational cost, posing great challenges if the model is large, especially in three-dimensional space. It is for this purpose that we proposed the surface contact formulation.

As shown in Figure 2, in the surface contact formulation, the interaction force acting on an infinitesimal element $da_1 \in \partial\Omega_1$ due to the presence of $da_2 \in \partial\Omega_2$ can be expressed as

$$d\mathbf{F}_1 = (\beta_1 \beta_2 (\mathbf{n}_2 \otimes \mathbf{r}_{12}) \cdot \mathbf{n}_1 \psi(s))\, da_2 da_1, \tag{4}$$

where $\mathbf{r}_{12} := \mathbf{r}_1 - \mathbf{r}_2$ is the vector pointing surface point $\mathbf{r}_2 \in \partial\Omega_2$ to $\mathbf{r}_1 \in \partial\Omega_1$. The scalar s is the length of the position vector $\mathbf{r}_{12}$, and the potential $\psi(r)$ is given as

DOI: 10.1002/nme

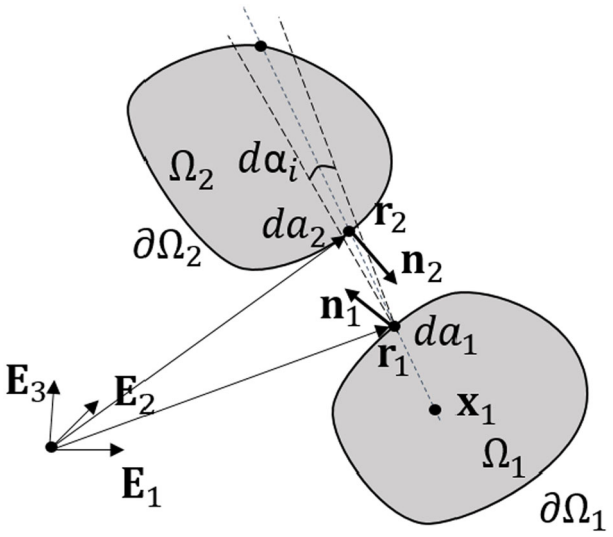

Figure 2. The surface integral scheme for the adhesive contact model.

$$\psi(r) = \frac{1}{r^3}\int_r^\infty \phi(t)t^2\,dt, r > 0 \tag{5}$$

By making use of the Nanson formula $\mathbf{n}da = J\mathbf{F}^{-T}\mathbf{N}dA$ [25], Equation (4) can also be rewritten in terms of quantities in the reference configuration,

$$d\mathbf{F}_1 = \left\{\beta_{10}\beta_{20}\left[\left(\mathbf{F}^{-T}\mathbf{N}_2\right)\otimes\mathbf{r}_{12}\right]\cdot\left(\mathbf{F}^{-T}\mathbf{N}_1\right)\psi(s)\right\}dA_2dA_1, \tag{6}$$

where β_{10}, β_{20} are the particle densities and dA_2, dA_1 the infinitesimal surface element areas.

Similarly, the interaction force applying on an infinitesimal surface element $da_2 \in \partial\Omega_2$ due to the presence of an infinitesimal surface element $da_1 \in \partial\Omega_1$ can be obtained as

$$d\mathbf{F}_2 = (\beta_1\beta_2(\mathbf{n}_1\otimes\mathbf{r}_{21})\cdot\mathbf{n}_2\psi(s))\,da_1da_2, \tag{7}$$

and

$$d\mathbf{F}_2 = \left\{\beta_{10}\beta_{20}\left[\left(\mathbf{F}^{-T}\mathbf{N}_1\right)\otimes\mathbf{r}_{21}\right]\cdot\left(\mathbf{F}^{-T}\mathbf{N}_2\right)\psi(s)\right\}dA_1dA_2, \tag{8}$$

3. SURFACE STRESS TENSOR AND ITS APPLICATIONS

From Equations (4) and (7), one can obtain

$$\frac{d\mathbf{F}_1}{da_1} = [\beta_1\beta_2(\mathbf{n}_2\otimes\mathbf{r}_{12})\psi(s)da_2]\cdot\mathbf{n}_1 \tag{9}$$

and

$$\frac{d\mathbf{F}_2}{da_2} = [\beta_1\beta_2(\mathbf{n}_1\otimes\mathbf{r}_{21})\psi(s)da_1]\cdot\mathbf{n}_2 \tag{10}$$

If one defines

$$d\mathbf{t}_I^s := \frac{d\mathbf{F}_I}{da_I}, \quad d\boldsymbol{\sigma}_I^s := \beta_I\beta_J(\mathbf{n}_J\otimes\mathbf{r}_{IJ})\psi(s)da_J, \;\; I,J = 1,2, I \neq J \tag{11}$$

DOI: 10.1002/nme

then Equations (9) and (10) can be written as

$$d\mathbf{t}_I^s = d\boldsymbol{\sigma}_I^s \mathbf{n}_I \tag{12}$$

where $d\boldsymbol{\sigma}_I^s$ and $d\mathbf{t}_I^s$ are the infinitesimal surface stress tensor and the corresponding traction force on $\partial\Omega_I$. If we perform the integration over the surface $\partial\Omega_J$, we may arrive at a new quantity,

$$\boldsymbol{\sigma}_I^s = \int_{\partial\Omega_J} d\boldsymbol{\sigma}_I^s = \int_{\partial\Omega_J} \beta_I \beta_J (\mathbf{n}_J \otimes \mathbf{r}_{IJ}) \psi(s) da_J, \quad I = 1, 2 \tag{13}$$

which represents the surface stress tensor at point $\mathbf{x}_I \in \partial\Omega_I$, due to the total interaction from body Ω_J. The corresponding surface traction at point $\mathbf{x}_I \in \partial\Omega_I$ can then be expressed as

$$\mathbf{t}_I^s = \boldsymbol{\sigma}_I^s \mathbf{n}_I, \quad I = 1, 2 \tag{14}$$

If one of the two interacting bodies is rigid, we can perform the integration of Equation (13) analytically for a given interatomic potential $\phi(r)$ and then apply the surface stress tensor to the numerical computation directly. For instance, for the 12-6 Lennard-Jones potential given by Equation (2), if body Ω_J is a rigid sphere with radius R as shown in Figure 3, the surface stress tensor can be derived as a diagonal tensor (as what will be used in one numerical example),

$$\boldsymbol{\sigma}_I^s = \sigma_{Ixx}^s \mathbf{e}_x \otimes \mathbf{e}_x + \sigma_{Iyy}^s \mathbf{e}_y \otimes \mathbf{e}_y + \sigma_{Izz}^s \mathbf{e}_z \otimes \mathbf{e}_z \tag{15}$$

where

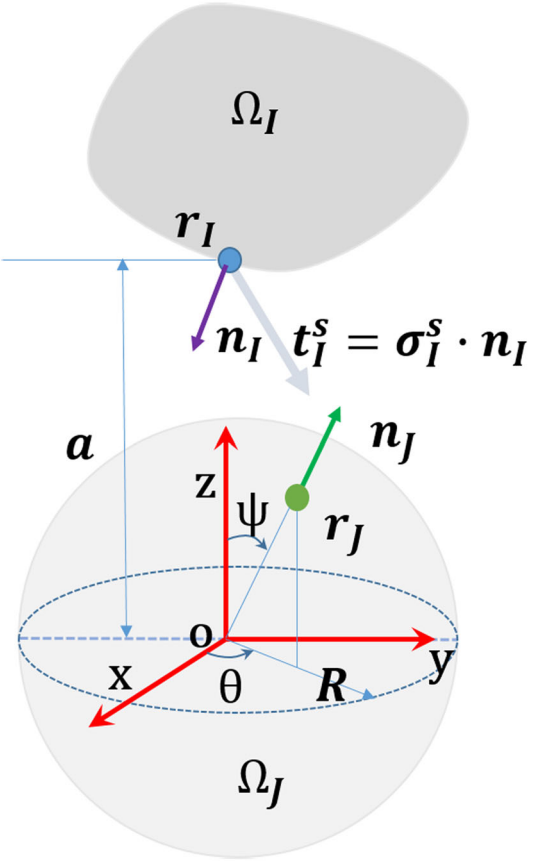

Figure 3. Surface stress tensor of a rigid sphere.

DOI: 10.1002/nme

$$\sigma^s_{Ixx} = \sigma^s_{Iyy} = \pi\beta_I\beta_J\varepsilon\sigma_0^6 \left\{ \frac{4\left(5a^4 + 14a^2R^2 + 5R^4\right)R^3}{135\left(a-R\right)^8\left(a+R\right)^8}\sigma_0^6 + \frac{\left(a^2+R^2\right)R}{3a^2\left(a^2-R^2\right)^2} - \frac{1}{12a^3}\ln\left[\left(\frac{a-R}{a+R}\right)^2\right]\right\}; \tag{16}$$

$$\sigma^s_{Izz} = \pi\beta_I\beta_J\varepsilon\sigma_0^6 \left\{ -\frac{4R^3\left(55a^6 + 207a^4R^2 + 117a^2R^4 + 5R^6\right)}{135\left(a-R\right)^9\left(a+R\right)^9}\sigma_0^6 + \frac{2\left(a^4 + 4a^2R^2 - R^4\right)R}{3a^2\left(a-R\right)^3\left(a+R\right)^3} + \frac{1}{6a^3}\ln\left[\frac{(a-R)^2}{(a+R)^2}\right]\right\}, \tag{17}$$

in which a is the shortest distance of the surface particle $\mathbf{r}_I$ to the center of the rigid sphere. The vectors $\mathbf{e}_x, \mathbf{e}_y$ and $\mathbf{e}_z$ are defined to be the unit vector along the corresponding axis.

With the surface stress tensor, one can easily compute the contact interaction force for the deformable body. For quasi-static analysis, the corresponding contact stiffness matrix can also be obtained with no technique difficulty.

A main advantage of the surface stress tensor formulation is that it can be used to convert the complicated adhesive contact problem, which is a non-standard boundary-value problem, to the conventional boundary value problem of continuum mechanics. That is,

$$\begin{cases} \dfrac{\partial \boldsymbol{\sigma}_I}{\partial \mathbf{x}_I} + \mathbf{b}_I = \mathbf{0}, & \text{in} \quad \Omega_I, \quad I = 1,2 \\ \mathbf{u}_I = \bar{\mathbf{u}}_{I0}, & \text{on} \quad \partial\Omega_{Iu}, \quad I = 1,2 \\ \boldsymbol{\sigma}^s_I \mathbf{n}_I = \bar{\mathbf{t}}_{I0}, & \text{on} \quad \partial\Omega_{I_t}, \quad I = 1,2 \\ \boldsymbol{\sigma}^s_I \mathbf{n}_I = \mathbf{t}^s_I, & \text{on} \quad \partial\Omega_{I_{at}}, \quad I = 1,2 \end{cases} \tag{18}$$

where the adhesive surface traction is determined in Equations (13) and (14).

4. GALERKIN WEAK FORMULATION AND FINITE ELEMENT DISCRETIZATION

In this section, the Galerkin weak formulation of the adhesive contact problem with the proposed surface formulation is first presented. Using a standard FEM approach [26, 27], the discretized approximation displacement fields are applied to the weak form from which the global mass matrix, internal force vector, external force vector, and the contact force vector are identified.

For the contact interaction system in Figure 1, the variation of the internal energy $\Pi^{int,I}$ for body Ω_I can be expressed as

$$\delta\Pi^{int,I} = \int_{\Omega_I} \boldsymbol{\sigma}_I : \frac{\partial \delta \mathbf{u}_I}{\partial \mathbf{x}_I} dv_I \tag{19}$$

For a conservative system, the variation of the external potential energy for body Ω_I is given by

$$\delta\Pi^{ext,I} = -\int_{\Omega_I} \rho_I \mathbf{b}_I \cdot \delta\mathbf{u}_I dv_I - \int_{\partial\Omega_{IT}} \mathbf{t}_I \cdot \delta\mathbf{u}_I ds, \tag{20}$$

where $\rho_I, \mathbf{b}_I$ are the mass density and body force in Ω_I and $\mathbf{t}_I$ represents the traction force on the Neumann boundary $\partial\Omega_{IT}$. The first variation of the contact interaction energy $\Pi^{C,s}$ can be expressed as

$$\delta\Pi^{C,s} = \int_{\partial\Omega_1}\int_{\partial\Omega_2} \beta_1\beta_2 \left[(\mathbf{n}_2 \otimes \mathbf{r}_{12}) \cdot \mathbf{n}_1 \psi(s) \cdot \delta\mathbf{u}_1 + \mathbf{n}_1 \otimes \mathbf{r}_{21}) \cdot \mathbf{n}_2 \psi(s) \cdot \delta\mathbf{u}_2\right] da_2 da_1. \tag{21}$$

DOI: 10.1002/nme

Collecting the terms of Equations (19)–(21) and replacing the body force $\mathbf{b}_I$ with $(\mathbf{b}_I - \dot{\mathbf{v}}_I)$, the principle of the stationary potential energy yields the following Galerkin weak form,

$$\sum_{I=1}^{2}\left[\int_{\Omega_I}\rho_I\dot{\mathbf{v}}_I\delta\mathbf{u}_I dv_I + \int_{\Omega_I}\boldsymbol{\sigma}_I : \frac{\partial\delta\mathbf{u}_I}{\partial\mathbf{x}_I}dv_I\right] + \int_{\partial\Omega_1}\int_{\partial\Omega_2}\beta_1\beta_2\left[(\mathbf{n}_2\otimes\mathbf{r}_{12})\cdot\mathbf{n}_1\psi(s)\cdot\delta\mathbf{u}_1 + (\mathbf{n}_1\otimes\mathbf{r}_{21})\cdot\mathbf{n}_2\psi(s)\cdot\delta\mathbf{u}_2\right]da_2da_1 = \sum_{I=1}^{2}\left[\int_{\Omega_I}\rho_I\mathbf{b}_I\cdot\delta\mathbf{u}_I dv_I + \int_{\partial\Omega_{IT}}\mathbf{t}_I\cdot\delta\mathbf{u}_I ds\right], \quad \forall\delta\mathbf{u}_I, I = 1,2 \tag{22}$$

where $\mathbf{v}_I = \dot{\mathbf{u}}_I$ is the velocity field in body Ω_I.

Consider the following interpolations of the displacement field $\mathbf{u}_I$ and the corresponding variation $\delta\mathbf{u}_I$ for body Ω_I,

$$\mathbf{u}_I(\mathbf{x}) = \sum_{A=1}^{n_{node}} N_I^A(\mathbf{x})\mathbf{d}_I^A, \quad I = 1,2 \tag{23}$$

and

$$\delta\mathbf{u}_I(\mathbf{x}) = \sum_{A=1}^{n_{node}} N_I^A(\mathbf{x})\delta\mathbf{d}_I^A, \quad I = 1,2 \tag{24}$$

where n_{node} denotes the number of nodes in the system, $N^A(\mathbf{x})$ is the finite element shape function associated with node A, and $\mathbf{d}_I^A$ and $\delta\mathbf{d}_I^A$ are the displacement and the corresponding variation at node A. Practically, Equations (23) and (24) are expressed element-wisely, i.e.

$$\mathbf{u}_I(\mathbf{x})|_{\Omega_I^e} = \sum_{A=1}^{n_{en}} N_I^A(\mathbf{x})\mathbf{d}_I^A \quad I = 1,2 \tag{25}$$

and

$$\delta\mathbf{u}_I(\mathbf{x})|_{\Omega_I^e} = \sum_{A=1}^{n_{en}} N_I^A(\mathbf{x})\delta\mathbf{d}_I^A \quad I = 1,2 \tag{26}$$

where n_{en} is the number of nodes for each element.

By substituting Equations (25) and (26) into Equation (22) and reorganizing, one can obtain

$$\begin{aligned}&\sum_{I=1}^{2}\sum_{iel=1}^{n_{elem}}\sum_{A=1}^{n_{en}}\sum_{B=1}^{n_{en}}\delta\mathbf{d}_I^A\cdot\int_{\Omega_I^e}\rho_I N_I^A N_I^B\ddot{\mathbf{d}}_I^B dv_I + \sum_{I=1}^{2}\sum_{iel=1}^{n_{elem}}\sum_{A=1}^{n_{en}}\delta\mathbf{d}_I^A\cdot\int_{\Omega_I^e}\boldsymbol{\sigma}_I\frac{\partial N_I^A}{\partial\mathbf{x}_I}dv_I\\ &-\sum_{I=1}^{2}\sum_{iel=1}^{n_{elem}}\sum_{A=1}^{n_{en}}\delta\mathbf{d}_I^A\cdot\int_{\Omega_I^e}\rho_I N_I^A\mathbf{b}_I dv_I - \sum_{I=1}^{2}\sum_{iel=1}^{n_{elem}}\sum_{A=1}^{n_{en}}\delta\mathbf{d}_I^A\cdot\int_{\partial\Omega_{TI}^e}N_I^A\mathbf{t}_I ds_I\\ &+\sum_{I=1}^{2}\sum_{isel=1}^{n_{selem1}}\sum_{jsel=1}^{n_{selem2}}\sum_{A=1}^{n_{sen}}\int_{\partial\Omega_1^e}\int_{\partial\Omega_2^e}\beta_1\beta_2 N_I^A(\mathbf{n}_J\otimes\mathbf{r}_{IJ})\cdot\mathbf{n}_I\psi(s)da_2da_1, \quad I = 1,2\end{aligned} \tag{27}$$

which is essentially

$$\delta\mathbf{d}_I\cdot\left(\mathbf{M}_I\ddot{\mathbf{d}}_I + \mathbf{f}_I^{int} + \mathbf{f}_I^{cont} - \mathbf{f}_I^{ext}\right) = 0, \quad I = 1,2 \tag{28}$$

where we have defined the following quantities

DOI: 10.1002/nme

$$\mathbf{M}_I = \sum_{iel=1}^{n_{elem}} \sum_{A=1}^{n_{en}} \sum_{B=1}^{n_{en}} \int_{\Omega_I^e} \rho_I N_I^A N_I^B dv_I \tag{29}$$

$$\mathbf{f}_I^{int} = \sum_{iel=1}^{n_{elem}} \sum_{A=1}^{n_{en}} \int_{\Omega_I^e} \boldsymbol{\sigma}_I \frac{\partial N_I^A}{\partial \mathbf{x}_I} dv_I \tag{30}$$

$$\mathbf{f}_I^{ext} = \sum_{iel=1}^{n_{elem}} \sum_{A=1}^{n_{en}} \int_{\Omega_I^e} \rho_I N_I^A \mathbf{b}_I dv_I + \sum_{iel=1}^{n_{elem}} \sum_{A=1}^{n_{en}} \int_{\partial\Omega_{TI}^e} N_I^A \mathbf{t}_I ds_I \tag{31}$$

$$\mathbf{f}_I^{cont} = \sum_{isel=1}^{n_{selem1}} \sum_{jsel=1}^{n_{selem2}} \sum_{A=1}^{n_{sen}} \int_{\partial\Omega_1^e} \int_{\partial\Omega_2^e} \beta_1 \beta_2 N_I^A (\mathbf{n}_J \otimes \mathbf{r}_{IJ}) \cdot \mathbf{n}_I \psi(s) da_2 da_1, \;\; I, J = 1, 2, \;\; I \neq J, \tag{32}$$

in which n_{selem1} and n_{selem2} are the total number of surface elements on $\partial\Omega_1$ and $\partial\Omega_2$, respectively, n_{sen} is the number of nodes for each surface element, $\mathbf{n}_I$ and $\mathbf{n}_J$ are the unit surface out-normal at corresponding surface points $\mathbf{r}_I \in \partial\Omega_I$ and $\mathbf{r}_J \in \partial\Omega_J$, and $\mathbf{r}_{IJ} = \mathbf{r}_I - \mathbf{r}_J$ is the vector pointing from $\mathbf{r}_I$ to $\mathbf{r}_J$. Because of the arbitrariness of the variation $\delta\mathbf{d}_I$, Equation (28) can be reduced to

$$\mathbf{M}_I \ddot{\mathbf{d}}_I + \mathbf{f}_I^{int} + \mathbf{f}_I^{cont} - \mathbf{f}_I^{ext} = \mathbf{0}, \;\; I = 1, 2 \tag{33}$$

which are the discretized equations of motion of the system.

5. CONTACT TANGENT STIFFNESS MATRIX

In this section, we provide the complete derivation of the tangent stiffness matrices for the contact interaction force corresponding to the surface stress tensor formulation of nonlinear continua under finite deformation.

Before proceeding, we first introduce the directional or Gâteaux derivative of a general nonlinear function $f(\mathbf{x}_i)$ in the direction of $\Delta\mathbf{x}_i = \Delta\mathbf{u}_i$,

$$D_{\Delta\mathbf{u}_i} f(x_i) = \lim_{\eta \to 0} \frac{f(\mathbf{x}_i + \eta\Delta\mathbf{u}_i) - f(\mathbf{x}_i)}{\eta} = \left. \frac{df(\mathbf{x}_i + \eta\Delta\mathbf{u}_i)}{d\eta} \right|_{\eta=0}, \;\; i = 1, 2 \tag{34}$$

where η is a scalar parameter and $\Delta\mathbf{u}_i$ is a kinematically admissible variation of the displacement field that satisfies the homogeneous essential boundary conditions on $\partial_{\mathbf{u}}\Omega_i$.

The variation of the contact interaction potential or the contact virtual work $\delta\Pi_e^{C,s}$ for the interaction of two surface elements $\partial\Omega_1^e \in \partial\Omega_1$ and $\partial\Omega_2^e \in \partial\Omega_2$ can be expressed in the reference configuration as

$$\begin{aligned} \delta\Pi_e^{C,s} = \int_{\partial\Omega_{10}^e} \int_{\partial\Omega_{20}^e} \beta_{10}\beta_{20} \{ &\left[\left(\mathbf{F}_2^{-T} \mathbf{N}_2 \right) \otimes \mathbf{r}_{12} \right] \cdot \left(\mathbf{F}_1^{-T} \mathbf{N}_1 \right) \psi(s) \cdot \delta\mathbf{u}_1 \\ &+ \left[\left(\mathbf{F}_1^{-T} \mathbf{N}_1 \right) \otimes \mathbf{r}_{21} \right] \cdot \left(\mathbf{F}_2^{-T} \mathbf{N}_2 \right) \psi(s) \cdot \delta\mathbf{u}_2 \} \, dA_2 dA_1 \end{aligned} \tag{35}$$

To obtain the corresponding tangent stiffness matrix, we take the Gâteaux derivative of $\delta\Pi_e^{C,s}$ in the direction of $\Delta\mathbf{u}_i$ for the two bodies in the form of

$$\Delta_{\mathbf{x}_1} \left(\delta\Pi_e^{C,s} \right) = D_{\Delta\mathbf{u}_1} \delta\Pi_e^{C,s}(\mathbf{x}_1, \mathbf{x}_2) \Delta\mathbf{u}_1 = \delta\mathbf{d}_1^T \mathbf{ke}_{11}^{cont,s} \Delta\mathbf{d}_1 + \delta\mathbf{d}_2^T \mathbf{ke}_{21}^{cont,s} \Delta\mathbf{d}_1 \tag{36}$$

DOI: 10.1002/nme

and

$$\Delta_{\mathbf{x}_2}\left(\delta\Pi_e^{C,s}\right) = D_{\Delta\mathbf{u}_2}\delta\Pi_e^{C,s}(\mathbf{x}_1,\mathbf{x}_2)\Delta\mathbf{u}_2 = \delta\mathbf{d}_1^T\mathbf{ke}_{12}^{cont,s}\Delta\mathbf{d}_2 + \delta\mathbf{d}_2^T\mathbf{ke}_{22}^{cont,s}\Delta\mathbf{d}_2, \tag{37}$$

in which $\delta\mathbf{u}_i = \mathbf{N}^i\delta\mathbf{d}^i, \Delta\mathbf{u}_i = \mathbf{N}^i\Delta\mathbf{d}^i, i = 1,2$.

By taking the directional derivative in the direction of displacement variation $\Delta\mathbf{u}_1$ in body 1, we find that

$$\begin{aligned}\Delta_{\mathbf{x}_1}\left(\delta\Pi_e^{C,s}\right) = &\int_{\partial\Omega_{10}^e}\int_{\partial\Omega_{20}^e}\beta_{10}\beta_{20}\delta\mathbf{u}_1\cdot\left\{\left(\mathbf{F}_2^{-T}\mathbf{N}_2\right)\otimes\frac{\partial\left[\mathbf{r}_{12}\cdot\left(\mathbf{F}_1^{-T}\mathbf{N}_1\right)\right]}{\partial\mathbf{x}_1}\psi(s)\right.\\ &\left.+\left[\mathbf{r}_{12}\cdot\left(\mathbf{F}_1^{-T}\mathbf{N}_1\right)\right]\left(\mathbf{F}_2^{-T}\mathbf{N}_2\right)\otimes\frac{\partial\psi(s)}{\partial\mathbf{x}_1}\right\}\cdot\Delta\mathbf{u}_1 dA_2 dA_1\\ &+\int_{\partial\Omega_{10}^e}\int_{\partial\Omega_{20}^e}\beta_{10}\beta_{20}\delta\mathbf{u}_1\cdot\left\{\left[\mathbf{r}_{21}\cdot\left(\mathbf{F}_2^{-T}\mathbf{N}_2\right)\right]\psi(s)\frac{\partial\left(\mathbf{F}_1^{-T}\mathbf{N}_1\right)}{\partial\mathbf{x}_1}-\phi(s)\left(\mathbf{F}_1^{-T}\mathbf{N}_1\right)\right.\\ &\left.\otimes\left(\mathbf{F}_2^{-T}\mathbf{N}_2\right)+\left[\mathbf{r}_{21}\cdot\left(\mathbf{F}_2^{-T}\mathbf{N}_2\right)\right]\left(\mathbf{F}_1^{-T}\mathbf{N}_1\right)\otimes\frac{\partial\psi(s)}{\partial\mathbf{x}_1}\right\}\cdot\Delta\mathbf{u}_2 dA_2 dA_1\end{aligned} \tag{38}$$

In the aforementioned equation,

$$\frac{\partial\left[\mathbf{r}_{12}\cdot\left(\mathbf{F}_1^{-T}\mathbf{N}_1\right)\right]}{\partial\mathbf{x}_1} = \left(\frac{\partial\mathbf{r}_{12}}{\partial\mathbf{x}_1}\right)^T\left(\mathbf{F}_1^{-T}\mathbf{N}_1\right)+\left(\frac{\partial\left(\mathbf{F}_1^{-T}\mathbf{N}_1\right)}{\partial\mathbf{x}_1}\right)^T\mathbf{r}_{12} \tag{39}$$

and

$$\frac{\partial\psi(s)}{\partial\mathbf{x}_1} = \frac{\partial\psi(s)}{\partial s}\frac{\partial s}{\partial\mathbf{x}_1} = \frac{\partial\psi(s)}{\partial s}\frac{\mathbf{r}_{12}}{s} \tag{40}$$

In Equation (39),

$$\frac{\partial\mathbf{r}_{12}}{\partial\mathbf{x}_1} = \mathbf{I} \tag{41}$$

and

$$\left(\frac{\partial\left(\mathbf{F}_1^{-T}\mathbf{N}_1\right)}{\partial\mathbf{x}_1}\right)^T\mathbf{r}_{12} = (\mathbf{r}_{12}\otimes\mathbf{N}_1):\frac{\partial\mathbf{F}_1^{-T}}{\partial\mathbf{x}_1}+\left(\frac{\partial\mathbf{N}_1}{\partial\mathbf{x}_1}\right)^T\left(\mathbf{F}_1^{-1}\mathbf{r}_{12}\right) \tag{42}$$

where

$$\frac{\partial\mathbf{N}_1}{\partial\mathbf{x}_1} = \frac{\partial\mathbf{N}_1}{\partial\mathbf{X}_1}\mathbf{F}_1^{-1} \tag{43}$$

The derivative $\frac{\partial\mathbf{F}_1^{-1}}{\partial\mathbf{x}_1}$ can be obtained in the following way

$$\begin{aligned} F_{Bi}^{-1}F_{iC} &= \delta_{BC}\\ \Rightarrow \frac{\partial F_{Bi}^{-1}}{\partial X_A}F_{iC}+F_{Bi}^{-1}\frac{\partial F_{iC}}{\partial X_A} &= 0\\ \Rightarrow \frac{\partial F_{Bi}^{-1}}{\partial X_A} &= -F_{Bk}^{-1}\frac{\partial F_{kC}}{\partial X_A}F_{Ci}^{-1}\\ \Rightarrow \frac{\partial F_{Bi}^{-1}}{\partial x_j} &= -F_{Bk}^{-1}\mathcal{G}_{kCA}F_{Ci}^{-1}F_{Aj}^{-1}\end{aligned} \tag{44}$$

DOI: 10.1002/nme

where

$$G_{kCA} = \frac{\partial F_{kC}}{\partial X_A} = \frac{\partial^2 x_k}{\partial X_C \partial X_A} \tag{45}$$

Substitute both Equations (39)–(43) and the finite element approximations $\delta\mathbf{u}_1 = \mathbf{N}^1\delta\mathbf{d}_1$; $\delta\mathbf{u}_2 = \mathbf{N}^2\delta\mathbf{d}_1$; $\Delta\mathbf{u}_1 = \mathbf{N}^1\Delta\mathbf{d}_1$ into Equation (38). After a few manipulations, one can obtain

$$\begin{aligned}\Delta_{\mathbf{x}_1}(\delta\Pi_e^{C,s}) = \delta\mathbf{d}_1^T &\left\{\int_{\partial\Omega_{10}^e}\int_{\partial\Omega_{20}^e}\mathbf{N}^1\mathbf{k}_{11}^s\mathbf{N}^1 dA_2 dA_1\right\}\Delta\mathbf{d}_1 \\ &+ \delta\mathbf{d}_2^T\left\{\int_{\partial\Omega_{10}^e}\int_{\partial\Omega_{20}^e}\mathbf{N}^2\mathbf{k}_{21}^s\mathbf{N}^1 dA_2 dA_1\right\}\Delta\mathbf{d}_1,\end{aligned} \tag{46}$$

where the matrices $\mathbf{k}_{11}^s$ and $\mathbf{k}_{21}^s$ are defined as

$$\begin{aligned}\mathbf{k}_{11}^s = \left(\mathbf{F}_2^{-T}\mathbf{N}_2\right)\otimes&\left[\mathbf{F}_1^{-T}\mathbf{N}_1 + (\mathbf{r}_{12}\otimes\mathbf{N}_1) : \frac{\partial\mathbf{F}_1^{-T}}{\partial\mathbf{x}_1} + \mathbf{F}_1^{-T}\left(\frac{\partial\mathbf{N}_1}{\partial\mathbf{X}_1}\right)^T\left(\mathbf{F}_1^{-1}\mathbf{r}_{12}\right)\right]\psi(s) \\ &+ \left[\mathbf{r}_{12}\cdot\left(\mathbf{F}_1^{-T}\mathbf{N}_1\right)\right]\frac{\partial\psi(s)}{\partial s}\frac{1}{s}\left(\mathbf{F}_2^{-T}\mathbf{N}_2\right)\otimes\mathbf{r}_{12}\end{aligned} \tag{47}$$

and

$$\begin{aligned}\mathbf{k}_{21}^s = &\left[\mathbf{r}_{21}\cdot\left(\mathbf{F}_2^{-T}\mathbf{N}_2\right)\right]\psi(s)\left(\mathbf{F}_1^{-T}\frac{\partial\mathbf{N}_1}{\partial\mathbf{X}_1} + \mathbf{N}_1\cdot\frac{\partial\mathbf{F}_1^{-1}}{\partial\mathbf{X}_1}\right)\mathbf{F}_1^{-1} - \psi(s)\left(\mathbf{F}_1^{-T}\mathbf{N}_1\right)\otimes\left(\mathbf{F}_2^{-T}\mathbf{N}_2\right) \\ &+ \left[\mathbf{r}_{21}\cdot\left(\mathbf{F}_2^{-T}\mathbf{N}_2\right)\right]\frac{\partial\psi(s)}{\partial s}\frac{1}{s}\left(\mathbf{F}_1^{-T}\mathbf{N}_1\right)\otimes\mathbf{r}_{12}\end{aligned} \tag{48}$$

By comparing Equation (46) with Equation (36), one can easily see that

$$\mathbf{ke}_{11}^{cont,s} = \int_{\partial\Omega_{10}^e}\int_{\partial\Omega_{20}^e}\mathbf{N}^1\mathbf{k}_{11}^s\mathbf{N}^1 dA_2 dA_1 \tag{49}$$

and

$$\mathbf{ke}_{21}^{cont,s} = \int_{\partial\Omega_{10}^e}\int_{\partial\Omega_{20}^e}\mathbf{N}^2\mathbf{k}_{21}^s\mathbf{N}^1 dA_2 dA_1 \tag{50}$$

Using exactly the same approach, one can obtain

$$\mathbf{ke}_{12}^{cont,s} = \int_{\partial\Omega_{10}^e}\int_{\partial\Omega_{20}^e}\mathbf{N}^1\mathbf{k}_{12}^s\mathbf{N}^2 dA_2 dA_1 \tag{51}$$

and

$$\mathbf{ke}_{22}^{cont,s} = \int_{\partial\Omega_{10}^e}\int_{\partial\Omega_{20}^e}\mathbf{N}^2\mathbf{k}_{22}^s\mathbf{N}^2 dA_2 dA_1 \tag{52}$$

where the two other matrices $\mathbf{k}_{12}^s$ and $\mathbf{k}_{22}^s$ are defined as

$$\begin{aligned}\mathbf{k}_{12}^s = &\left[\mathbf{r}_{12}\cdot\left(\mathbf{F}_1^{-T}\mathbf{N}_1\right)\right]\psi(s)\left(\mathbf{F}_2^{-T}\frac{\partial\mathbf{N}_2}{\partial\mathbf{X}_2} + \mathbf{N}_2\cdot\frac{\partial\mathbf{F}_2^{-1}}{\partial\mathbf{X}_2}\right)\mathbf{F}_2^{-1} - \psi(s)\left(\mathbf{F}_2^{-T}\mathbf{N}_2\right)\otimes\left(\mathbf{F}_1^{-T}\mathbf{N}_1\right) \\ &+ \left[\mathbf{r}_{12}\cdot\left(\mathbf{F}_1^{-T}\mathbf{N}_1\right)\right]\frac{\partial\psi(s)}{\partial s}\frac{1}{s}\left(\mathbf{F}_2^{-T}\mathbf{N}_2\right)\otimes\mathbf{r}_{21}\end{aligned} \tag{53}$$

DOI: 10.1002/nme

and

$$\mathbf{k}_{22}^{s} = \left(\mathbf{F}_1^{-T}\mathbf{N}_1\right) \otimes \left[\mathbf{F}_2^{-T}\mathbf{N}_2 + (\mathbf{r}_{21} \otimes \mathbf{N}_2) : \frac{\partial \mathbf{F}_2^{-T}}{\partial \mathbf{x}_2} + \mathbf{F}_2^{-T}\left(\frac{\partial \mathbf{N}_2}{\partial \mathbf{X}_2}\right)^{T}\left(\mathbf{F}_2^{-1}\mathbf{r}_{21}\right)\right]\psi(s) + \left[\mathbf{r}_{21} \cdot \left(\mathbf{F}_2^{-T}\mathbf{N}_2\right)\right]\frac{\partial \psi(s)}{\partial s}\frac{1}{s}\left(\mathbf{F}_1^{-T}\mathbf{N}_1\right) \otimes \mathbf{r}_{21} \tag{54}$$

We would like to point out that in the aforementioned equations, $\mathbf{N}_i$ and $\mathbf{N}^i$ $(i = 1, 2)$ represent completely different quantities. $\mathbf{N}_i$ is the unit surface out-normal on $\partial\Omega_i^e$ in the reference configuration, while $\mathbf{N}^i$ denotes the element shape function matrix for Ω_i^e.

6. NUMERICAL EXAMPLES AND DISCUSSIONS

In this section, several numerical examples are presented to show the accuracy, efficiency, and reliability of the proposed surface formulation for three-dimensional adhesive contact. Three different types of constitutive relations for the bulk material are used in these numerical calculations, namely, the Neo-Hookean material model, the St. Venant–Kirchhoff material model, and the Newtonian fluid model. The strain energy density function W of a compressible Neo-Hookean material used in the numerical example is expressed as follows

$$W = \frac{1}{2}\mu(I_1 - 3 - 2\ln J) + \frac{1}{2}\lambda(J-1)^2 \tag{55}$$

where λ and μ are the lame constants. I_1 is the trace of the right Cauchy-Green tensor $\mathbf{C}$ and J is the determinant of the deformation gradient $\mathbf{F}$. The free-energy density function for the St. Venant–Kirchhoff material model used in the numerical example is given by

$$W(\mathbf{E}) = \frac{\lambda}{2}(\mathrm{tr}\,\mathbf{E})^2 + \mu \mathrm{tr}\,\mathbf{E}^2 \tag{56}$$

where $\mathbf{E}$ is the Green–Lagrange strain tensor and λ and μ are the Lame constants. The constitutive equation for the Newtonian fluid used in the numerical calculation is

$$\boldsymbol{\sigma} = -p\mathbf{I} + 2\mu\mathbf{d}, \tag{57}$$

where $p = \kappa(J-1)$ is the hydrostatic pressure, κ is bulk modulus, μ is the viscosity, and $\mathbf{d}$ is the rate of deformation.

In addition, the contact interaction between any two particles from distinctive bodies are governed by the 12-6 Lennard-Jones potential in Equation (2). Unless specifically provided, the equilibrium distance is σ_0, the potential well is ε, and the atomic density of the two bodies are $\beta_{10} = \beta_{20} = \beta_0$.

6.1. Accuracy of the finite element discretization

The first example serves as a testing example to assess the discretization errors introduced by the finite element approximation. The contact interaction forces resulting from numerical integration for different integration schemes and different meshes are investigated. To be specific, we are considering the interaction between a half-hollow cylinder and a cubic block, as shown in Figure 4. The inner radii, outer radii, and the height of the cylinder are chosen as $r_i = \sigma_0, r_o = 2.0\sigma_0$, and $H = 8.0\sigma_0$. The side length of the cubic block is set as $a = 4.0\sigma_0$. The closest distance between any two points in the two bodies is denoted as d. The center of the cubic block and that of the hollow cylinder are both on the z axis. The two bodies are discretized by eight-node hexahedron elements, as shown in Figure 5(a). We are only interested in the finite element discretization error in the evaluation of the total contact interaction forces with respect to the volume integration (VI) and surface integration (SI) approaches. Three different meshes are considered, with the total number of elements being 1239, 2087, and 4472.

DOI: 10.1002/nme

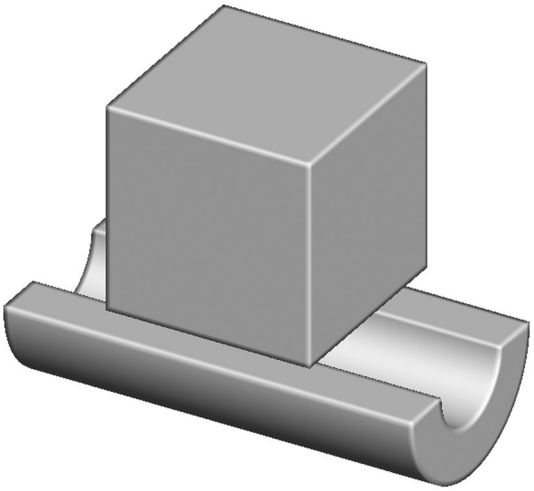

Figure 4. Interaction between a half-hollow cylinder and a cubic block.

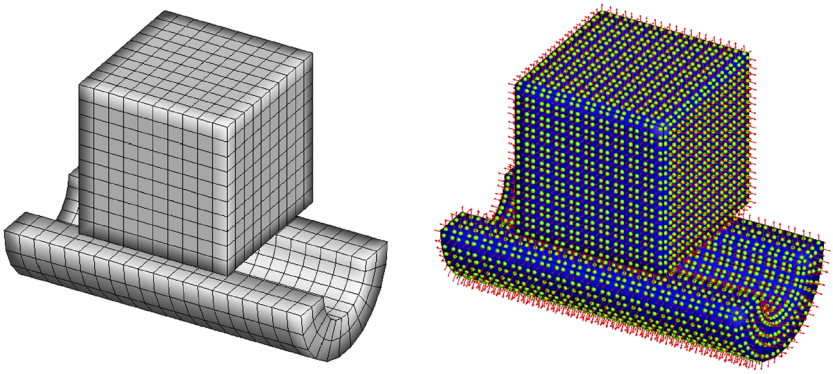

(a) mesh discretization (b) initial unit out-normals

Figure 5. Interaction between a half-hollow cylinder and a cubic block. (a) mesh discretization. (b) initial unit out-normals.

For the SI approach, the coordinate, unit surface out-normal, and integration weight associated with any surface Gauss integration point are needed in order to evaluate the contact interaction force. As shown in 5(b), these quantities are obtained using the technique presented in [22]. The dots (green online) are the positions of the integration points, and the arrow (red online) denotes the direction of the corresponding unit out-normal.

To better evaluate the discretization errors, a series of distance d are considered. We want to emphasize that, here, the two bodies are always considered to be rigid and motionless. The total interaction forces of the two bodies versus the distance d for different meshes and different integration schemes are shown in Figure 6 (a)–(c). The three different schemes are (1) VI with 2^3 integration points in each bulk element; (2) VI with 4^3 integration points in each bulk element; and (3) SI with 2^2 integration points in each surface element. The 'exact' total interaction forces are obtained from a mesh size of $\Delta = 0.02\sigma_0$. As can be seen, the general trends of these curves obtained from the two different schemes are the same, resembling the force displacement relation of the 12-6 Lennard-Jones potential (Equation (2)), which to some extent shows that the surface integration scheme proposed is correct. For the surface integration scheme, the error percentages of the total interaction forces versus the distances for the three different meshes are plotted in Figure 7, from which one can tell that the total interaction forces for the surface integration scheme are always less than 6%.

DOI: 10.1002/nme

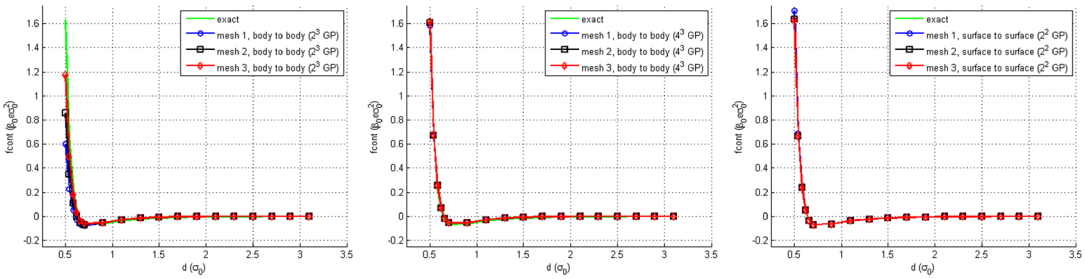

(a) VI with 2^3 GPs per bulk element

(b) VI with 4^3 GPs per bulk element

(c) SI with 2^2 GPs per surface element

Figure 6. The contact interaction force versus the shortest distance of the two bodies. (a) VI with 2^3 Gauss integration per bulk element; (b) VI with 4^3 Gauss integration points per bulk element; and (c) SI with 2^2 Gauss integration points per surface element.

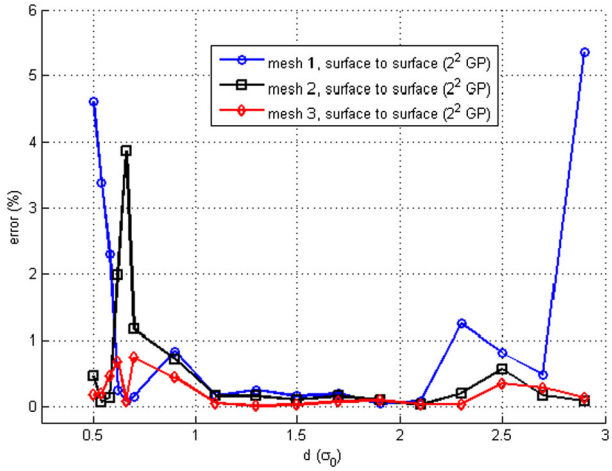

Figure 7. Error percentage of the contact interaction force for the surface integration scheme.

Table I. Error percentage and computation time for the total contact interaction force of the two bodies at $d = 0.5\sigma_0$.

	VI (2^3 GPs)		VI (4^3 GPs)		SI (2^2 GPs)	
Mesh1	63.31%	2.4 s	2.82%	138.95 s	4.61%	0.90 s
Mesh2	47.29%	7.22 s	1.38%	417.18 s	0.46%	2.07 s
Mesh3	27.87%	42.74 s	0.69%	2435.91 s	0.17%	6.68 s

VI, volume integration; SI, surface integration; GPs, Gauss integration points.
The computation is carried out in an Intel Core i7-4700HQ processor.

To take a closer look at the errors produced by the three different schemes, the errors at the distance $d = 0.5\sigma_0$ are shown in Table I. One can see that the errors for the first scheme VI–2^3 are at least 27% for the three different meshes, while the errors for the other two schemes are always lower than 6%. Meanwhile, by comparing the simulation time it takes to compute the total contact interaction forces, one can tell that the third scheme SI–2^2 is the most efficient.

6.2. Nanoindentation

In this section, the quasi-static analysis of a nanoindentation model problem is presented to demonstrate the capability of the proposed surface contact formulation in the case when one of the interacting bodies is rigid. We are considering the indentation of a hyperelastic block by a rigid

DOI: 10.1002/nme

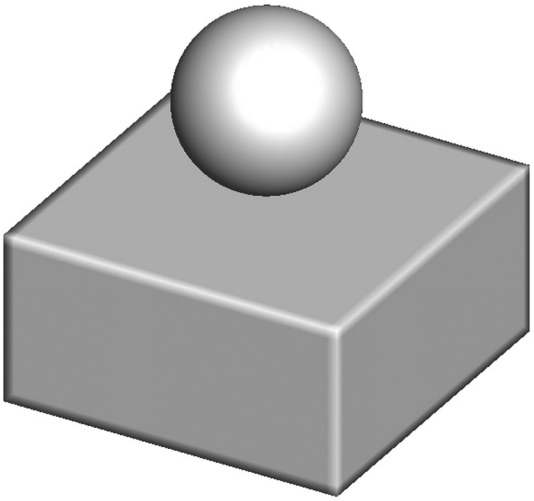

Figure 8. Nanoindentation of a rigid sphere on a hyperelastic substrate.

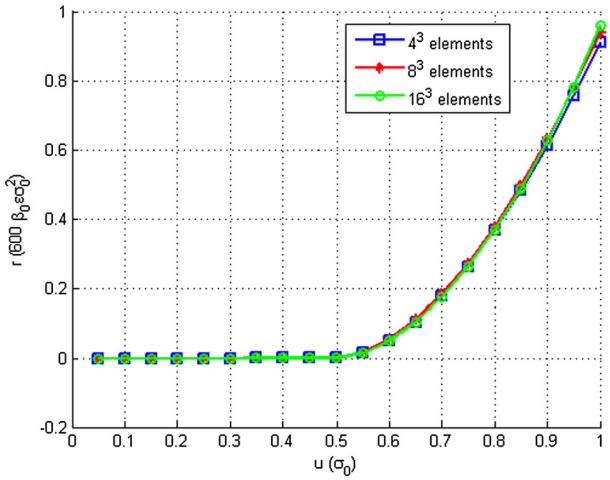

Figure 9. Nanoindentation: reaction force versus the prescribed displacement.

sphere, as shown in Figure 8. The Neo-Hookean model is taken as the constitutive relation of the block, with the Young's modulus $E = 1000\beta_0\varepsilon$ and Poisson's ratio $\nu = 0.25$. The dimension of the block is $4\sigma_0 \times 4\sigma_0 \times 2\sigma_0$. The radius of the rigid sphere is $R = 1.2\sigma_0$. The rigid sphere is prescribed with displacement in the vertical direction. The top surface of the block is free, and the other five surfaces are fixed in the normal direction. Initially, the shortest distance between the sphere and the block is $3.2\sigma_0$. The contact interaction forces between the elastic block and the rigid sphere are obtained by using the surface stress tensor in Equation (3). A corresponding reduced contact stiffness matrix is included into the formulation. The expression for the reduced contact stiffness matrix is very long and therefore omitted here. The 2×2 surface integration scheme is adopted for the evaluation of the contact interaction force in the block.

Figure 9 shows the reaction force versus the prescribed displacement for three different meshes. The three curves present small gaps, but are in the same trend. Initially, the rigid sphere is far away and the reaction force is zero. As the rigid sphere is gradually pushed into the block, the reaction forces increase. For a fixed prescribed displacement, the finer the mesh, the larger the reaction force, which is expected, because at the same physical region, the surface Gauss integration points are in general closer to the rigid sphere for the case of a finer mesh. Figure 10 shows the trace of the

DOI: 10.1002/nme

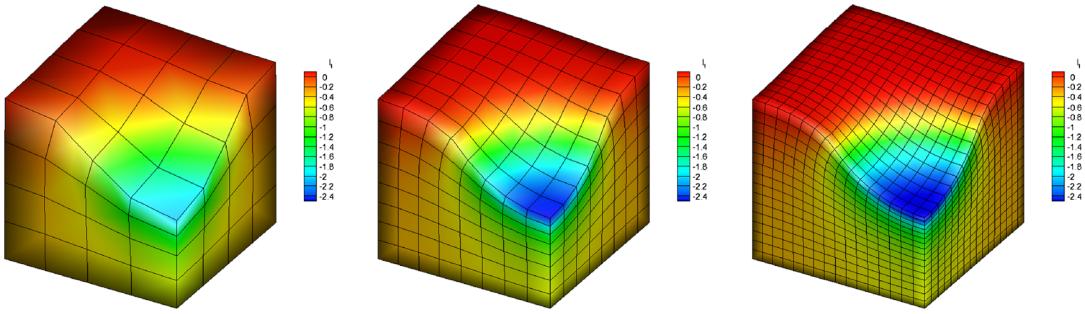

(a) 4^3 elements (b) 8^3 elements (c) 16^3 elements

Figure 10. The contour shows the trace of the stress tensor in the hyperelastic block. (a) 4^3 elements. (b) 8^3 elements. (c) 16^3 elements.

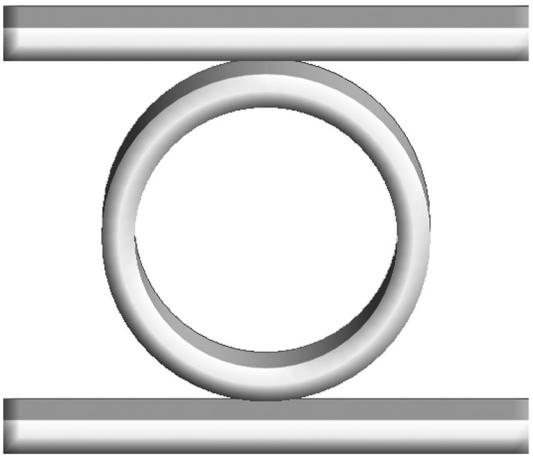

Figure 11. Pressing of an elastic ring: schematic of the problem.

stress tensor $I_1 = \mathrm{tr}(\boldsymbol{\sigma})$ distribution at $u = 2.0\sigma_0$ for the three different meshes. One can see that the distribution patterns of I_1 for the three different cases are very similar except slight differences of the corresponding magnitudes. The finer the mesh, the higher the magnitude of I_1, due to the fact that a finer mesh would lead to a larger reaction force.

6.3. Pressing of an elastic ring

This example concerns the pressing of an elastic ring by two elastic slabs in three-dimensional space, which is shown in Figure 11. The inner radii, outer radii, and side length of the elastic ring are $16.0\sigma_0$, $20.0\sigma_0$, and $24.0\sigma_0$. The two elastic slabs are identical and of the dimension $64.0\sigma_0 \times 32.0\sigma_0 \times 4.0\sigma_0$. The axis of the 3D elastic ring is always parallel to the y axis. Initially, the gap between the ring and the block is $d = 2.0\sigma_0$. By exploring symmetry, only one-eighth of the problem is considered. Both the ring and the block are modeled by the Neo-Hookean material and are discretized by an eight-node hexahedron element. The material properties of the ring and slab are Young's modulus $E_r = 25\beta_0\sigma_0$, $E_s = 0.05\beta_0\sigma_0$ and Poisson's ratio $\nu_r = \nu_s = 0.25$. A quasi-static simulation is performed by prescribing the top of the one-eighth elastic ring in the negative z direction with a total displacement $u_z = -6.4\sigma_0$ in 32 increments. The bottom of the slab is fixed with zero displacement. Two different integration schemes are considered: the body-to-body integration with 3^3 Gauss integration points in each bulk element (VI–3^3 GPs) and the surface-to-surface integration with 2^2 Gauss integration points in each surface element (SI–2^2 GPs). Figure 12 shows deformed shapes and the trace of the stress tensor distributions of the two bodies at the load step $u_z = -6.4\sigma_0$ for the two integration schemes. Although one may observe that the ring and the

DOI: 10.1002/nme

slab are slightly closer at the contact region for the surface integration scheme, the results from the two schemes are very close. To have a qualitative comparison, the trace of the stress tensor along the inner and outer ring is plotted in Figure 13. It can be seen that the two curves of the trace of the stress tensor along the inner ring are almost overlapped (Figure 13(a)). In fact, the other two curves for the trace of the stress tensor along the outer ring are also very close, only with a small gap near the contact region (Figure 13(b)). The magnitude of the trace of the stress tensor at contact region for the SI scheme is larger than that of the VI scheme. Both the differences of the deformed shapes and the trace of the stress tensor at the contact region are due to the fact the VI scheme makes use of the Gauss integration points in the bulk, while the SI scheme makes use of the Gauss integration points on the surface, which provides a 'stronger' interaction for the same geometry.

6.4. *Dynamic spreading of a nano-droplet over an elastic substrate*

Through this example, we hope to demonstrate the capability of the proposed surface formulation in describing the dynamic contact interaction between two arbitrarily shaped bodies undergoing finite deformations in three-dimensional space. To be specific, we are considering the dynamic spreading of a nanoscale droplet on a hyperelastic substrate, as shown in Figure 14(a). The parameters for the Lennard-Jones potential are $\beta_d = 33.3/nm^3$, $\beta_s = 60.662/nm^3$, $\sigma_0 = 1nm$, and $\varepsilon = 6.0 \times 10^{-22}J$. The radius of the droplet is $r = 5nm$, and the dimension of the cylinder substrate is radius $20nm$ and height $4.5nm$. The droplet is modeled as a Newtonian fluid, and the substrate is modeled as St. Venant–Kirchhoff material. The bulk modulus, viscosity, and density of the droplet

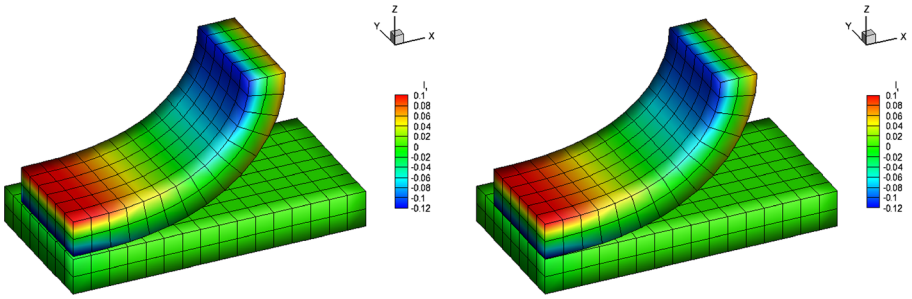

(a) The VI–3^3 scheme (b) The SI–2^2 scheme

Figure 12. Trace of the stress tensor ($I_1 = \mathrm{tr}(\boldsymbol{\sigma})$) distributions for the two different integration schemes at the load step $u_z = -6.4\sigma_0$. (a) the VI–3^3 scheme. (b) the SI–2^2 scheme.

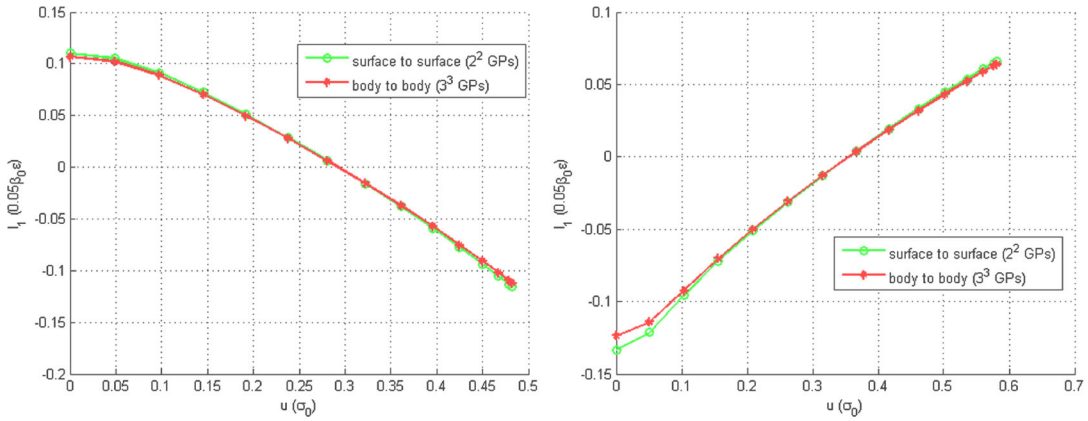

(a) Along the inner side of the ring (b) Along the outer side of the ring

Figure 13. Trace of the stress tensor ($I_1 = \mathrm{tr}(\boldsymbol{\sigma})$) comparisons for the two different integration schemes. (a) Along the inner side of the ring. (b) Along the outer side of the ring.

DOI: 10.1002/nme

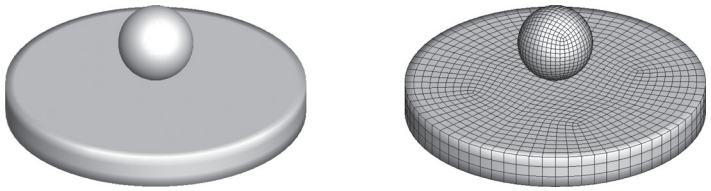

(a) schematic of the problem (b) mesh discretization

Figure 14. Dynamic spreading of a nano-droplet on an elastic substrate. (a) schematic of the problem. (b) mesh discretization.

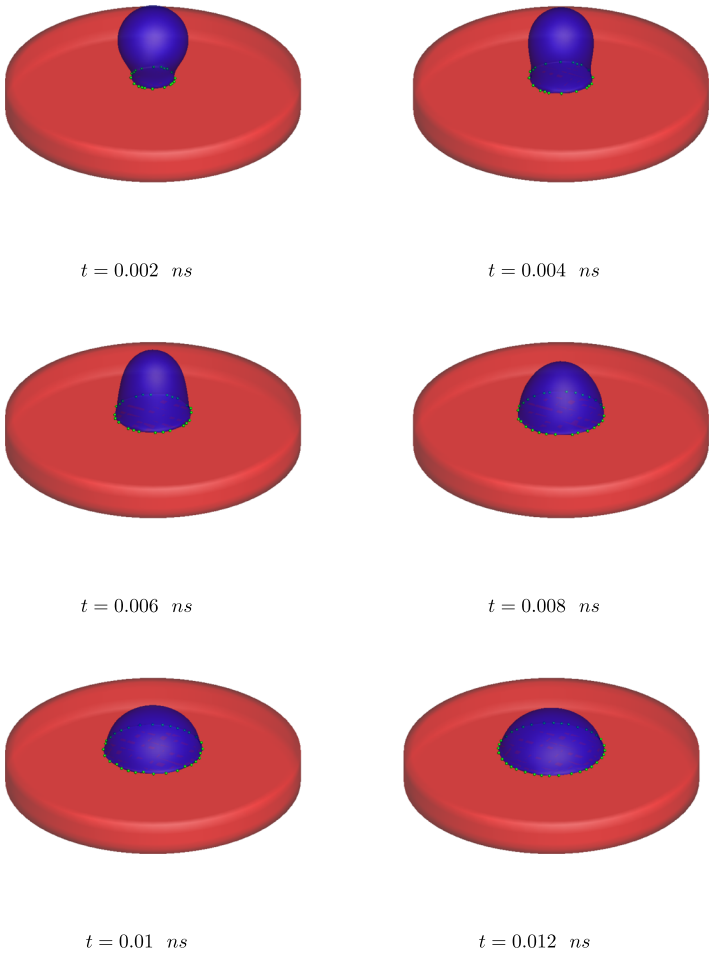

Figure 15. Time sequence of the droplet spreading upon the elastic substrate. The dots (green online) denotes the current position of the moving contact line.

is $\kappa = 2.2 \times 10^9 Pa$, $\mu = 1.8 \times 10^{-4} Pa \cdot s$, and $\rho_d = 1.0 \times 10^3 kg/m^3$. The Young's modulus, Poisson's ratio, and density of the substrate are $E = 1.2 \times 10^8 Pa$, $\nu = 0.40$, and $\rho_s = 8.94 \times 10^3 kg/m^3$. In the simulation, the droplet and the substrate are discretized into 4341 and 3072 eight-node brick elements, as shown in Figure 14(b). The 2×2 surface integration scheme is adopted for the evaluation of the contact interaction force between the droplet and the substrate. The surface tension between water and the atmosphere is $\gamma = 7.275 \times 10^{-2}\ N/m$. The contact angle is set to be 60°. Details of how to incorporate the surface tension effect can be found in [28–30]. The total simulation time is $T = 2.5 \times 10^{-11} s$ with the time step $dt = 1.25 \times 10^{-15} s$. Figure 15 shows a time

DOI: 10.1002/nme

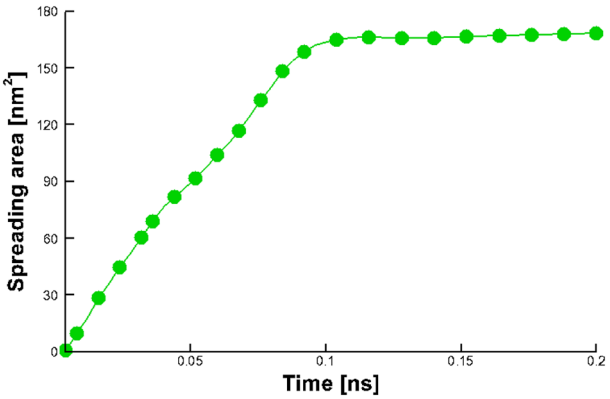

Figure 16. Time evolution of the droplet-spreading area.

sequence of the droplet-spreading process on the substrate. The droplet first adheres to the elastic substrate, owing to the adhesion effect. After the initial contact, the surface tension effect, especially the effect at the moving contact line, comes into place [28]. The combination of the adhesion and surface tension drives the natural spreading of the droplet. We would like to mention that during the whole simulation, no gravitational force is considered and the main driving force is the adhesion between the droplet and the substrate. The time evolution of the droplet spreading area is shown in Figure 16. One can see that the droplet first increases rapidly (owing to the initial adhesive contact), and then the combination of the surface tension and the adhesive contact makes the droplet gradually spread further.

7. CONCLUSION

In this work, we present an adhesive surface stress formulation for solving three-dimensional adhesive contact problem under finite deformation. The adhesive contact is modeled by using the inter-molecular van der Waals force interaction potential, and it is used to calculate the contact surface cohesive force for nonlinear continua. A generalized Derjaguin type of approximation is used to construct the contact surface stress formula, and it is used to evaluate cohesive surface force between two deformable continuum bodies. We have demonstrated that the adhesive contact surface formulation provides an efficient and accurate means to describe macroscopic adhesive contact interaction between arbitrarily shaped deformable solids. The formulation of adhesive surface stress tensor is introduced and implemented in the nonlinear finite element formulation. In addition, the surface stress tensor for a perfect sphere is also obtained through analytical integration.

Several numerical examples are presented. The first example provides an estimate for the accuracy of the finite element surface approximation for the contact interaction forces of two adjacent bodies. It is revealed that the proposed surface contact formulation is reliable and efficient for the evaluation of the adhesive contact interaction forces. The second example uses the surface stress tensor formulation for a rigid sphere to simulate nanoindentation. Numerical results indicate that surface stress tensor formulation can accurately solve three-dimensional contact problems, and it greatly reduces computational cost and time. The third example is a simulation of an elastic ring being pressed by two slabs. It shows that the surface stress tensor formulation of the adhesive contact can accurately describe the contact interaction between two arbitrarily shaped and deformable objects. The last example demonstrates the capability of the surface stress tensor formulation for simulation of dynamics adhesive contact problems in three-dimensional space, and the simulation results show that it can accurately capture dynamic and transient effects.

ACKNOWLEDGEMENT

H. Fan is partially supported by graduate fellowships from the Chinese Scholar Council (CSC). This support is gratefully appreciated.

DOI: 10.1002/nme

REFERENCES

1. Wriggers P. *Computational Contact Mechanics*. Springer: Hannover, 2003.
2. Laursen TA. *Computational Contact and Impact Mechanics: Fundamentals of Modeling Interfacial Phenomena in Nonlinear Finite Element Analysis* (1st edn). Springer: Berlin, 2002.
3. Autumn K, Liang YA, Hsieh ST, Zesch W, Chan WP, Kenny TW, Fearing R, Full RJ. Adhesive force of a single gecko foot-hair. *Nature* 2000; **405**(6787):681–685.
4. Bhushan B. Adhesion of multi-level hierarchical attachment systems in gecko feet. *Journal of Adhesion Science and Technology* 2007; **21**(12-13):1213–1258.
5. Flachsbart BR, Wong K, Iannacone JM, Abante EN, Vlach RL, Rauchfuss PA, Bohn PW, Sweedler JV, Shannon MA. Design and fabrication of a multilayered polymer microfluidic chip with nanofluidic interconnects via adhesive contact printing. *Lab on a Chip* 2006; **6**(5):667–674.
6. Chen S, Gao H. Bio-inspired mechanics of reversible adhesion: orientation-dependent adhesion strength for non-slipping adhesive contact with transversely isotropic elastic materials. *Journal of the Mechanics and Physics of Solids* 2007; **55**(5):1001–1015.
7. Lin YY, Hui CY, Jagota A. The role of viscoelastic adhesive contact in the sintering of polymeric particles. *Journal of Colloid and Interface Science* 2001; **237**(2):267–282.
8. Johnson KL, Kendall K, Roberts AD. Surface energy and the contact of elastic solids. *Proceedings of the Royal Society A: Mathematical, Physical and Engineering Sciences* 1971; **324**(1558):301–313.
9. Derjaguin BV, Muller VM, Toporov YP. Effect of contact deformations on the adhesion of particles. *Journal of Colloid and Interface Science* 1975; **53**(2):314–326.
10. Allen MP, Tildesley DJ. *Computer Simulation of Liquids*. Oxford Science Publications: New York, 1989.
11. Frenkel D, Smit B. *Understanding Molecular Simulation: From Algorithms to Applications* (2nd edn). Academic Press: San Diego, 2001.
12. Andrew RL. *Molecular Modelling: Principles and Applications*. Prentice Hall (Pearson Education): Harlow, 2001.
13. Schlick T. *Molecular Modeling and Simulation: An Interdisciplinary Guide*. Springer: New York, 2002.
14. Gao G, Tahir C, III WAG. Energetics, structure, mechanical and vibrational properties of single-walled carbon nanotubes. *Nanoscale* 1998; **9**:184–191.
15. Hertel T, Walkup R, Avouris P. Deformation of carbon nanotubes by surface van der Waals forces. *Physical Review B* 1998; **58**(20):13870–13873.
16. Binnig G, Quate CF. Atomic force microscope. *Physical Review Letters* 1986; **56**(9):930–934.
17. Cappella B, Dietler G. Force-distance curves by atomic force microscopy. *Surface Science Reports* 1999; **34**(1-3): 1–104.
18. Lantz M, O'Shea SJ, Welland M. Simultaneous force and conduction measurements in atomic force microscopy. *Physical Review B* 1997; **56**(23):15345–15352.
19. Sauer RA, Li S. A contact mechanics model for quasi-continua. *International Journal for Numerical Methods in Engineering* 2007; **71**:931–962.
20. Sauer RA, Li S. An atomic interaction-based continuum model for adhesive contact mechanics. *Finite Elements in Analysis and Design* 2007; **43**(5):384–396.
21. Kloosterman G, Damme RMJV, van den Boogaard AH, Huetink J. A geometrical-based contact algorithm using a barrier method. *International Journal for Numerical Methods in Engineering* 2001; **51**(2000):865–882.
22. Fan H, Ren B, Li S. An adhesive contact mechanics formulation based on atomistically induced surface traction. *Journal of Computational Physics* 2015; **302**:420–438.
23. Argento C, Jagota A. Surface formulation for molecular interactions of macroscopic bodies. *Journal of the Mechanics and Physics of Solids* 1997; **45**:1161–1183.
24. Jagota A, Argento C. An intersurface stress tensor. *Journal of Colloid and Interface Science* 1997; **191**(2):326–36.
25. Holzapfel GA. *Nonlinear Solid Mechanics*. Wiley: Chichester, 2000.
26. Bathe K. *Finite Element Procedures*. Prentice-Hall: Englewood Cliffs, NJ, 1996.
27. Hughes TJR. *The Finite Element Method: Linear Static and Dynamic Finite Element Analysis*. Dover Publications: New York, 2000.
28. Li S, Fan H. On multiscale moving contact line theory. *Proceedings of the Royal Society A* 2015; **471**(2179):197–220.
29. Minaki H, Li S. Multiscale modeling and simulation of dynamic wetting. *Computer Methods in Applied Mechanics and Engineering* 2014; **273**:273–302.
30. Fan H, Li S. Modeling microtubule cytoskeleton via an active liquid crystal elastomer model. *Computational Materials Science* 2015; **96**:559–566.

DOI: 10.1002/nme